

# $\beta$ -Ketoenamine-Linked Covalent Organic Frameworks Synthesized via Gel-to-Gel Monomer Exchange Reaction: From Aerogel Monoliths to Electrodes for Supercapacitors

Jesús Á. Martín-Illán, Laura Sierra, Ana Guillem-Navajas, José Antonio Suárez, Sergio Royuela, David Rodríguez-San-Miguel, Daniel Maspoch, Pilar Ocón, and Félix Zamora\*

Covalent organic frameworks (COFs) possess intrinsic nanoscale pores, limiting mass transport and impacting their utility in many applications, such as catalysis, supercapacitors, and gas storage, demanding efficient diffusion throughout the material. Hierarchical porous structures, integrating larger macropores with inherent micro-/meso-pores, facilitate rapid mass transport. Recently, the fabrication of aerogel monoliths is reported exclusively from imine-linked COFs, offering flexibility in aerogel composition. However, challenges in synthesizing robust  $\beta$ -ketoenamine-based COFs with comparable surface areas prompted innovative synthetic approaches. Leveraging the dynamic nature of COF bonds, in this work efficient monomer exchange from imine to partially  $\beta$ -ketoenamine-linked COFs within the gel phase is demonstrated. These aerogels can be transformed into electrodes using the compression technique. The new flexible electrodes-based  $\beta$ -ketoenamine-linked COF composites with C super P exhibit superior durability and redox activity. Through supercapacitor assembly, the  $\beta$ -ketoenamine-linked COF electrodes outperform their imine-based counterparts, showcasing enhanced capacitance ( $88 \text{ mF cm}^{-2}$ ) and stability at high current densities ( $2.0 \text{ mA cm}^{-2}$ ). These findings underscore the promise of  $\beta$ -ketoenamine-linked COFs for pseudocapacitor energy storage applications.

## 1. Introduction

Porous materials are promising candidates for applications in several key areas, such as energy,<sup>[1]</sup> catalysis,<sup>[2]</sup> and separation field.<sup>[3,4]</sup> They have seen significant development in the last decades, fuelled by the implementation of reticular chemistry, which rationally enables the design of new structures.<sup>[5,6]</sup> Among them, covalent organic frameworks (COFs) have drawn considerable interest due to their intrinsically porous and designable covalent structures, resulting in materials with highly tunable chemical functionalities, pore sizes, and geometries.<sup>[7]</sup> These crystalline organic polymers can thus be tailored to perform remarkably well in gas separation and storage, water purification, sensing, catalysis, energy generation, and storage.<sup>[8,9]</sup>

However, the intrinsic pore size in COFs is generally in the order of a few nanometres, resulting in poor and sluggish mass transport within the material. While this may not be an issue for some applications,

J. Á. Martín-Illán, A. Guillem-Navajas, S. Royuela, D. Rodríguez-San-Miguel, F. Zamora  
Departamento de Química Inorgánica  
Universidad Autónoma de Madrid  
Madrid 28049, Spain  
E-mail: [felix.zamora@uam.es](mailto:felix.zamora@uam.es)

L. Sierra, P. Ocón  
Departamento de Química-Física Aplicada  
Universidad Autónoma de Madrid  
Madrid 28049, Spain

J. A. Suárez, D. Maspoch  
Catalan Institute of Nanoscience and Nanotechnology (ICN2)  
Consejo Superior de Investigaciones Científicas sede central (CSIC)  
Barcelona Institute of Science and Technology (BIST)  
Campus UAB, Bellaterra, Barcelona 08193, Spain

D. Rodríguez-San-Miguel, F. Zamora  
Institute for Advanced Research in Chemical Sciences (IAdChem)  
Universidad Autónoma de Madrid  
Madrid 28049, Spain

D. Maspoch  
Institución Catalana de Investigación y Estudios Avanzados (ICREA)  
Pg. Lluís Companys 23, Barcelona 08010, Spain  
F. Zamora  
Condensed Matter Physics Center (IFIMAC)  
Universidad Autónoma de Madrid  
Madrid 28049, Spain

The ORCID identification number(s) for the author(s) of this article can be found under <https://doi.org/10.1002/adfm.202403567>

© 2024 The Authors. Advanced Functional Materials published by Wiley-VCH GmbH. This is an open access article under the terms of the [Creative Commons Attribution-NonCommercial](#) License, which permits use, distribution and reproduction in any medium, provided the original work is properly cited and is not used for commercial purposes.

DOI: 10.1002/adfm.202403567

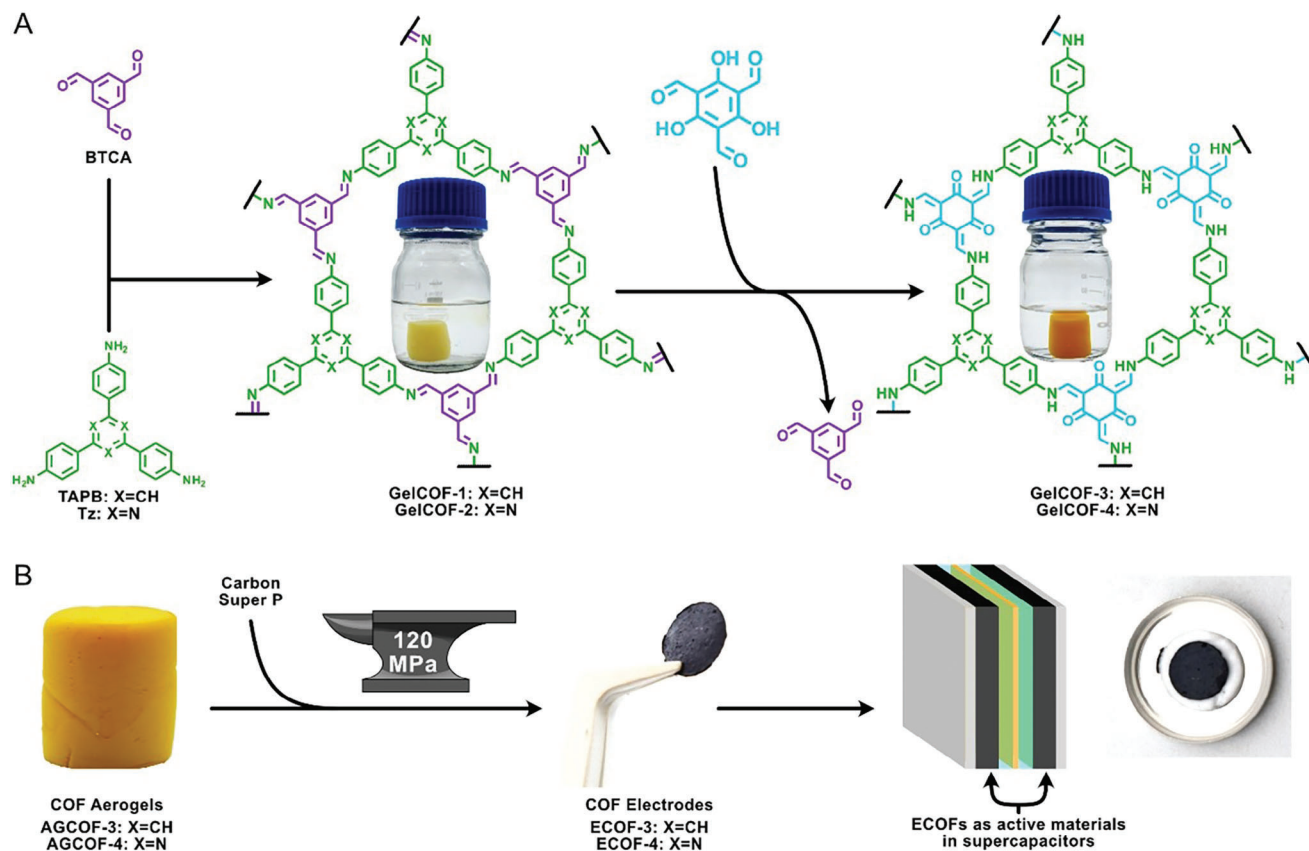


**Figure 1.** A) Schematic representation of the imine-linked COF gel synthesis and the gel-to-gel monomer exchange to obtain  $\beta$ -ketoenamine-linked gels. B) Schematic representation of the fabrication of supercapacitor electrodes from the  $\beta$ -ketoenamine-linked aerogels.

such as the optoelectronic ones, fast mass transport from the surface of the material to all its inner pores is critical to improve the performance of porous structures in catalysis, supercapacitors, and gas storage.<sup>[10,11]</sup> This faster diffusional rate can be achieved by fabricating hierarchical porous structures, where a system of macropores allows molecules easy access to most of the micro-/meso-pores intrinsic to the COF structure.

Several methods that generate this hierarchical structure have been recently reported, sometimes with the assistance of another material as a supporting matrix.<sup>[12–17]</sup> COF aerogels resulting from some of these methods add the benefit of being readily shaped into macroscopic objects (monoliths), which are easier to handle and more suited for some applications than powdered materials. In this area, we have recently reported the formation of aerogel monoliths composed solely of imine-linked COFs.<sup>[15]</sup> The process relies on the formation of a gel of the COF when the monomers react in acetic acid, which, upon a solvent exchange process, can be activated via CO<sub>2</sub> critical point drying, preserving both the microporosity, the macroporosity, and the shape of the initial gel. We could successfully prepare aerogels of various imine-linked COFs; however, other COF types, such as the more robust  $\beta$ -ketoenamine-based COFs, were unavailable with the current synthetic conditions.

This is unsurprising since  $\beta$ -ketoenamine-based COFs are usually difficult to obtain with surface areas as high as their imine-linked counterparts when using similar synthetic pro-

cesses. This has led to the development of novel routes to synthesize these COFs exhibiting high porosity. One of the most common approaches is the monomer exchange approach.<sup>[18]</sup> This process, based on the dynamic feature of the covalent bonds linking the COF framework, allows the substitution of building blocks of the COF, giving rise to a structural transformation into another COF structure. Despite the assumption that the extension of monomer substitution is close to quantitative, the reaction depends on several parameters (temperature, time, concentration, solvent...), and, indeed, it is not usually properly quantified. This work demonstrates, for the first time, that the monomer exchange process to transform an imine-linked COF into a partially  $\beta$ -ketoenamine-linked COF can occur efficiently in the gel form (**Figure 1**). This means that this process can be used to partially convert the initial imine-linked gel to a  $\beta$ -ketoenamine-linked gel, as a previous step to the formation of the corresponding monolithic  $\beta$ -ketoenamine-linked aerogels. Moreover, these aerogels can be transformed into electrodes by a simple compression method, which was also recently reported.<sup>[19]</sup> Using this method, we have fabricated a supercapacitor device to take advantage of the  $\beta$ -ketoenamine-linked COF aerogel superior features of robustness and redox-active sites. This supercapacitor shows an enhancement of the capacitance up to 88 mF cm<sup>-2</sup> and good stability at a high current density rate (2.0 mA cm<sup>-2</sup>), in comparison to the analogous imine-based COFs,<sup>[19]</sup> postulating these  $\beta$ -ketoenamine-linked

COF electrodes as candidates for pseudocapacitor energy storage applications.

## 2. Results and Discussion

In an initial step, we synthesized the imine-linked COF gels following our previously reported synthetic strategy, in which aldehyde (benzene-1,3,5-tricarbaldehyde, BTCA) and amine (1,3,5-tris(4-aminophenyl)benzene, TAPB, and 2,4,6-tris(4-aminophenyl)-1,3,5-triazine, TZ) monomers were dissolved in glacial acetic acid (AcOH) with water (10%, v/v) at mild conditions (Section S2.1, Supporting Information). The resultant monolithic gels corresponding to **TAPB-BTCA-COF** and **TZ-BTCA-COF**, hereafter named **gelCOF-1** and **gelCOF-2**, were then left undisturbed in AcOH for 5 days.<sup>[15]</sup> Next, the monomer exchange process was performed by dipping those imine-linked gels into a solution containing the monomer 2,4,6-trihydroxybenzene-1,3,5-tricarbaldehyde (Tp) in AcOH. Both gels were left in contact with the Tp solution for 3 days at mild conditions to allow the diffusion of the monomer over the gel (Section S2.2, Supporting Information). In this exchange process, the concentration of Tp was a critical parameter, as low concentrations resulted in a long exchange time. Indeed, we found that 3 equivalents of Tp per equivalent of BTCA were sufficient to shift the equilibrium and facilitate a rapid structural conversion. Interestingly, higher concentrations of the Tp exchange solution did not improve the exchange percentage (Table S1, Supporting Information).

After the monomer exchange process, tetrahydrofuran (THF) was used to remove the exchanged and unreacted monomers. Then, the solvent was exchanged with ethanol (EtOH) to obtain miscibility with the liquid CO<sub>2</sub>. Finally, supercritical CO<sub>2</sub> (scCO<sub>2</sub>) was used to activate the monolithic COF gels. The control of the venting rate of scCO<sub>2</sub> was critical to avoid a collapse of the porosity; thus, a proportional–integral–derivative (PID) controller system was integrated at the gas outlet, and the supercritical activation was performed by venting up ca. 8 bar h<sup>−1</sup> down to atmospheric pressure. This simple method gave rise to two novel COF aerogels, which we named **AGCOF-3** (resulting from the exchange of BTCA by Tp in **gelCOF-1**) and **AGCOF-4** (resulting from the exchange of BTCA by Tp in **gelCOF-2**). Control samples of the original imine aerogels were also prepared and isolated following this methodology, which led to pale yellow monoliths called **AGCOF-1** and **AGCOF-2** (obtained directly from **gelCOF-1** and **gelCOF-2**, respectively).

The extent of monomer exchange of both aerogels was evaluated using a hydrolysis-based approach, in which **AGCOF-3** and **AGCOF-4** were subjected to aggressive acid hydrolysis conditions (Section S2.3, Supporting Information). As a result, the imine bonds remaining after the exchange were hydrolyzed, and the constituent monomers were detected through <sup>1</sup>H NMR spectroscopy and quantified using an internal standard (Figures S6 and S7, Supporting Information). Fourier-transform infrared (FT-IR) analyses were performed on the solid obtained after the hydrolysis to confirm the total disappearance of the C=N stretching signal and verify the complete hydrolysis of the residual imine bonds within the aerogel present after the exchange (Figures S8 and S9, Supporting Information). This study confirms a degree of monomer exchange of 68% in **AGCOF-3**, mean-

ing that this percentage of imine bonds were converted to  $\beta$ -ketoenamine bonds during the monomer exchange process in the gel form. This value aligns with those values reported in the literature for this material.<sup>[18]</sup> It is crucial to emphasize that this monomer exchange procedure does not require harsh conditions, making these results even more noteworthy. On the other hand, **AGCOF-4** showed a degree of exchange of 77% (Table S1, Supporting Information).

A crystallographic study of both COF-aerogels was carried out by powder X-ray diffraction (PXRD). Diffraction patterns exhibited an excellent crystallinity, similar to the primary imine-based COF aerogels, and matched well with the simulated AA-eclipsed stacking models of the fully  $\beta$ -ketoenamine-linked COFs.<sup>[18,20–22]</sup> Thus, **AGCOF-3** showed an intense peak at 5.5° corresponding to the (100) plane, along with peaks at 9.8° and 11.3°, attributed to the (110) and (200) reflections, respectively (Figure 2B; S10, Supporting Information). Similarly, **AGCOF-4** displayed three peaks at 5.5°, 9.7°, and 11.3°, corresponding to the (100), (110), and (200) planes, respectively (Figure 2E; Figure S11, Supporting Information). A slight change in the peak intensity at ca. 9.8° attributed to (110) plane was observed in **AGCOF-3** and **AGCOF-4**, in concordance with the simulated pattern.<sup>[18]</sup> These results confirmed that the crystalline framework structure built in the primary COF-gel was held after monomer exchange.

After the monomer exchange, the aerogels experimented an evident change of color related to the  $\beta$ -ketoenamine bond formation. Both imine aerogels (**AGCOF-1** and **AGCOF-2**) changed color from light yellow to orange and bright yellow for **AGCOF-3** and **AGCOF-4**, respectively (Figure 2A,D). Accordingly, both aerogels showed a red shift in the UV–vis absorption spectra compared with the primary imine-linked COF-aerogels (Figures S12 and S13, Supporting Information). To further confirm the formation of the  $\beta$ -ketoenamine bonds in both COF aerogels, we performed FT-IR and <sup>13</sup>C cross-polarized magic angle spinning solid-state NMR (<sup>13</sup>C CP-MAS NMR) spectroscopies of the two new aerogels, and compared them to those of the corresponding imine-linked aerogels. In both **AGCOF-3** and **AGCOF-4**, FT-IR spectra showed an evident fading of the imine-linked stretching band at ca. 1698 cm<sup>−1</sup> and the presence of the enamine (C–N) stretching band at ca. 1290 cm<sup>−1</sup> (Figures S14 and S15, Supporting Information). In the <sup>13</sup>C CP-MAS NMR spectra, the exchanged COF aerogels showed the characteristic enamine carbon signal and the carbonyl carbon at 106 and 183 ppm for **AGCOF-3** (Figure 2C; Figure S16 and Table S2, Supporting Information) and at 108 and 185 ppm for **AGCOF-4** (Figure 2F; Figure S17 and Table S3, Supporting Information), respectively. Residual imine carbon signals and aromatic signals associated with the original BTCA aldehyde could also be observed due to the partial exchange of the monomers.

Interestingly, all synthesized  $\beta$ -ketoenamine-linked COF aerogels maintained most of the characteristics and properties of their imine-linked counterparts. From a morphological and microstructural point of view, they showed the characteristic sponge-like architectures made of nanolayers assembled into fiber-like structures, whose interconnection gives rise to hierarchical 3D aerogels (Figures S18 and S29, Supporting Information). Also, these aerogels kept their extremely low density (ca. 0.02 g cm<sup>−3</sup>) and thermal stability up to 500 °C (Figures S20 and S21, Supporting Information). Additionally,

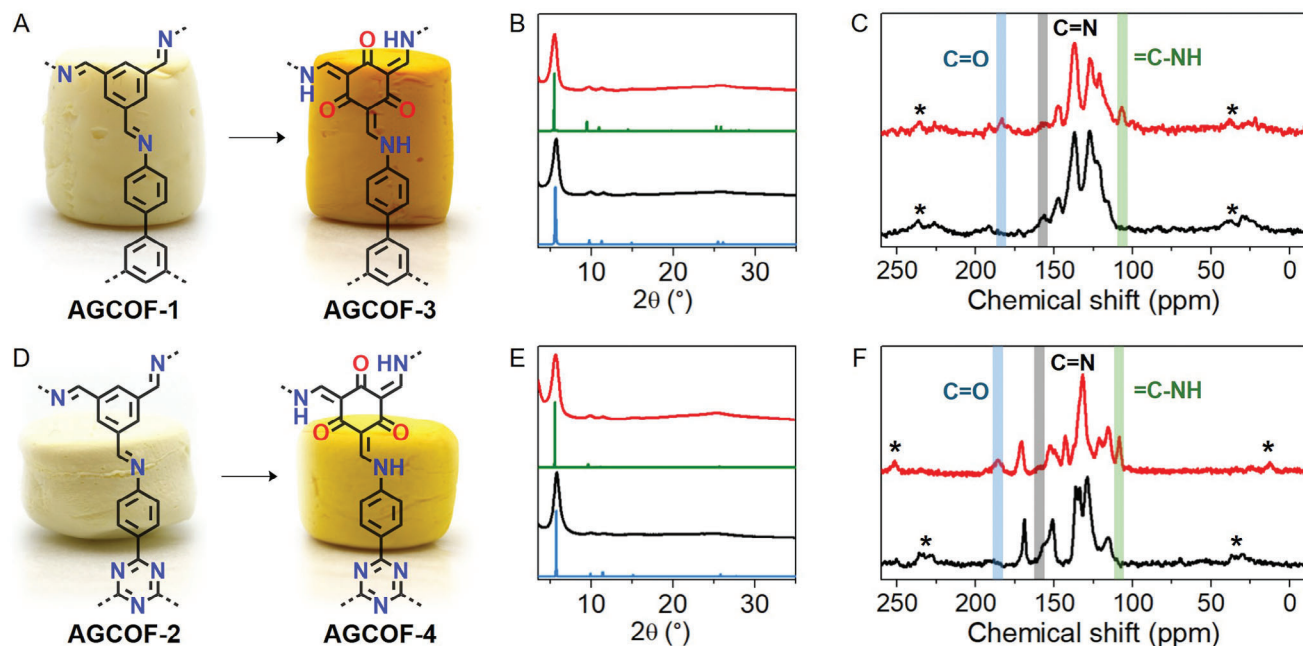


**Figure 2.** A) Photographs and structures of **AGCOF-1** and **AGCOF-3**. B) PXRD patterns of **AGCOF-1** (black), **AGCOF-3** (red), and their corresponding simulated patterns (blue and green, respectively). C)  $^{13}\text{C}$  CP-MAS NMR spectra of **AGCOF-1** (black), **AGCOF-3** (red). D) Photographs and structures of **AGCOF-2** and **AGCOF-4**. E) PXRD patterns of **AGCOF-2** (black), **AGCOF-4** (red), and their corresponding simulated patterns (blue and green, respectively). F)  $^{13}\text{C}$  CP-MAS NMR spectra of **AGCOF-2** (black), **AGCOF-4** (red). The carbonyl signal is highlighted in blue, the imine signal in grey, and the enamine signal in green.

the monomer exchange process did not affect their sorption capacities (Figures S22–S27, Supporting Information). Indeed,  $\text{N}_2$  adsorption isotherms at 77 K of the  $\beta$ -ketoenamine-linked COF aerogels showed typical type-II isotherms, as those of their imine-linked counterparts. We also calculated Brunauer–Emmett–Teller ( $S_{\text{BET}}$ ) surface areas of  $1064 \text{ m}^2 \text{ g}^{-1}$  for **AGCOF-3** and  $1383 \text{ m}^2 \text{ g}^{-1}$  for **AGCOF-4** from these isotherms. These values are close to those found for the original imine-linked aerogels ( $1146 \text{ m}^2 \text{ g}^{-1}$  for **AGCOF-1** and  $1368 \text{ m}^2 \text{ g}^{-1}$  for **AGCOF-2**),<sup>[19]</sup> thus confirming that the monomer exchange process performed under gel conditions allows for the generation of porous  $\beta$ -ketoenamine-linked COFs. The estimation of the pore-size distribution of all aerogels further confirmed the preservation of the intrinsic microporosity of the COFs, as evidenced by the presence of pores distributed  $\approx 1.3$ – $1.5 \text{ nm}$  (Figures S23 and S26, Supporting Information). Remarkably, additional  $\text{N}_2$  sorption measurements performed on these  $\beta$ -ketoenamine-linked aerogels after exposing them to atmospheric conditions for one week did not show a loss of sorption capacity, as was the case for the imine-linked aerogels.

Finally, the mechanical properties of the COF aerogels, evaluated through uniaxial quasi-static compression tests, were also preserved. Both the imine- and the  $\beta$ -ketoenamine-linked aerogels showed similar patterns in their stress-strain curves, beginning with an elastic region, where stress increases linearly with strain, and followed by a plastic region, where stress increases very rapidly, leading to a densification of the samples (Figures S28 and S29, Supporting Information). From the elastic region, Young's moduli were calculated and found to be in good agreement with those previously reported for **AGCOF-1** and

**AGCOF-2**.<sup>[15]</sup> Moreover, **AGCOF-3** and **AGCOF-4** also showed similar specific Young's moduli in the order of  $10^2 \text{ kPa cm}^3 \text{ g}^{-1}$  (Table S4, Supporting Information), further confirming that the microstructure of the materials is preserved after monomer exchange. The densification region starts at  $\approx 60\%$  strain, and all the aerogels can be easily compressed to 90% strain, transforming them into pellets. After the pressure was released, all the samples maintained excellent crystallinity (Figures S30 and S31, Supporting Information) and preserved their pellet-like shape.

Given this ability to transform our  $\beta$ -ketoenamine COF aerogels into pellets and their hierarchical pore structures, monolithic forms, hydrophobic nature, and high  $S_{\text{BET}}$  values, we were motivated to assess their potential as supercapacitors. In this article, we chose the amines TAPB and TZ to expand on the results obtained in our previous work with **AGCOF-1** and **AGCOF-2**,<sup>[19]</sup> where we observed a slight increase in capacitance when using an organic electrolyte in the case of the TZ structure. In this study, our objective is to extend this investigation by evaluating the capacitance of newly obtained  $\beta$ -ketoenamine-linked COF-based electrodes and examining the influence of the triazine ring on their performance. Furthermore, the  $\beta$ -ketoenamine backbones in these materials offer redox-active sites that enhance total capacitance. To fabricate the COF electrodes, we followed our previously established method (Section S1, Supporting Information).<sup>[19]</sup> Here, since the electrical conductivity of the pure COFs was too low to achieve excellent electrochemical performance, it was necessary to incorporate an additive in the electrode to enhance it. In this case, 30 wt.% Super P Carbon was mixed with **AGCOF-3** and **AGCOF-4** before pressing the mixture



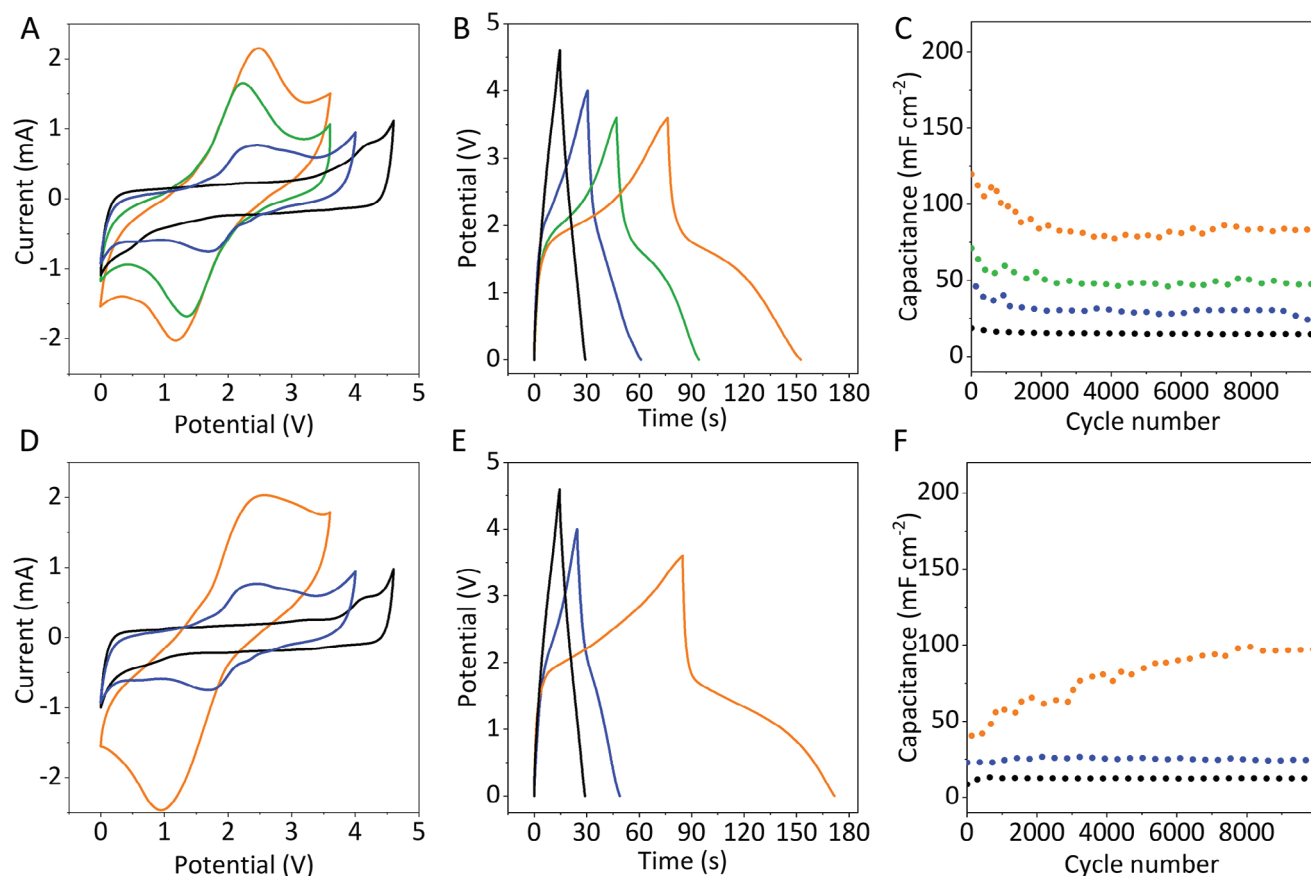


**Figure 3.** Cyclic voltammetry at  $50 \text{ mV s}^{-1}$  and  $25^\circ \text{C}$  with  $\text{TBABF}_4$  1 M in acetonitrile with different concentrations of TFA as electrolyte for **ECOF-3** A) and **ECOF-4** D). Galvanostatic charge-discharge profiles and cyclic stability at  $2.0 \text{ mA cm}^{-2}$  for **ECOF-3** B,C, respectively) and **ECOF-4** E,F, respectively). The black line corresponds to 0% TFA, the blue line to 5%, the green line to 10%, and the orange line to 20%.

into a pellet to fabricate electrodes **ECOF-3** and **ECOF-4**, respectively.

Cyclic voltammetry tests (CVs) were carried out to determine the potential window and the capacitive behavior of the ECOFs materials. **Figure 3A,D** illustrates the excellent behaviour of electrochemical double-layer capacitors (EDLC) of **ECOF-3** and **ECOF-4** electrodes in organic electrolyte without trifluoroacetic acid (TFA) additions. For both materials, the potential window was 4.6 V, where no redox peaks were observed. However, the capacitance value was small, slightly superior for **ECOF-3**,  $22 \text{ mF cm}^{-2}$ , than for **ECOF-4**,  $18 \text{ mF cm}^{-2}$ . To improve power and energy density, we tried to enhance the redox reactions associated with the reversible reaction of the keto-enol groups, which occur in the presence of protons. Thus, different amounts of TFA were added to the electrolyte. With a 5% TFA concentration, the potential window was reduced to 4.0 V (Figure 3A,D). Nevertheless, faradaic contributions associated with redox activity became evident, increasing the capacitance to 30 and  $27 \text{ mF cm}^{-2}$  for **ECOF-3** and **ECOF-4**, respectively. Increasing the TFA content to 10% and 20% was accompanied by a further decrease of the potential window to 3.6 V and an increase of the faradaic contributions. This resulted in capacitance values of  $54 \text{ mF cm}^{-2}$  for **ECOF-3** and  $61 \text{ mF cm}^{-2}$  for **ECOF-4** with 20% TFA, which shows the highest faradaic contribution.

In general, the CVs show us that the redox peaks increase with the addition of TFA, although a reduction in the potential window and the total power density is observed. As for the capacitance, its value increases significantly with the addition of TFA. The best performance for both electrodes **ECOF-3** and **ECOF-4** is observed with the addition of 20% of TFA, showing the best value of  $61 \text{ mF cm}^{-2}$  for **ECOF-4**.

CV tests were also performed for the corresponding imine-based COF electrodes (**ECOF-1** and **ECOF-2**) using the organic electrolyte with 20% TFA. The results show that the potential window is reduced from 4 to 1.3 V due to the absence of the redox peaks associated with the  $\text{C}=\text{O}$  moieties present in the  $\beta$ -ketoenamine-linked COFs (Figure S32, Supporting Information). Also, as it was previously mentioned, the lower stability of imine-based COF electrodes leads to a lower performance in terms of capacitance and energy density.

CVs of **ECOF-3** and **ECOF-4** were conducted at different scan rates without TFA and with 20% of TFA (Figure S33, Supporting Information). The same trend, a decrease in capacitance with increasing scan rate, was observed for both electrolytes and COFs, independently of the presence of Faradaic reactions (Table S5, Supporting Information). Even though the redox peaks at high scan rates are less evident, the values obtained with the addition of TFA were always higher for any scan rate.

To further confirm the stability and reliability of the devices, galvanostatic charge-discharge (GCD) tests were performed with symmetric cells. Figure 3B,E compares GCD profiles at a constant current rate of  $2.0 \text{ mA cm}^{-2}$  in cycle 10,000 with the different amounts of TFA. The measurement of the electrolyte with 0% TFA showed a symmetrical and nearly triangular potential-time curve without redox peaks for both structures. The capacitance values were 15 and  $13 \text{ mF cm}^{-2}$  for **ECOF-3** and **ECOF-4**, respectively. It is interesting to note that the analogous imine-based COFs showed values of 3.59 and  $5.12 \text{ mF cm}^{-2}$ , achieving an improvement in the capacitance of the material in organic electrolytes even without taking advantage of the faradaic processes exclusive of  $\beta$ -ketoenamine COFs.<sup>[19]</sup>

With the addition of 5% of TFA, the curves were no longer completely triangular due to the contribution of the faradaic reaction, and the capacitance increased to 30 and  $27 \text{ mF cm}^{-2}$  for **ECOF-3** and **ECOF-4**, respectively. Following the increase of TFA concentration up to 20%, the curves showed a more evident contribution of the faradaic reaction, and the capacitance continued to increase up to 82 and  $88 \text{ mF cm}^{-2}$  for **ECOF-3** and **ECOF-4**, respectively. This trend confirms that the best composition for high capacitance is 20% of TFA in the electrolyte. On the other hand, the energy and power values were estimated using the GCD essays (Table S6, Supporting Information). These parameters are essential in energy storage devices since, in addition to obtaining high capacitance, it is also necessary to get high energy and power density values. These parameters depend on the stability of the potential window; hence, devices with 0% TFA showed power values of 1.00 and  $0.98 \text{ W cm}^{-3}$  for **ECOF-3** and **ECOF-4**, respectively, while the power values for 20% TFA content decreased to 0.71 and  $0.70 \text{ W cm}^{-3}$ , respectively. On the other hand, the energy values were higher for the electrolyte with 20% TFA 14.8 and  $15.8 \text{ mWh cm}^{-3}$  for **ECOF-3** and **ECOF-4**, respectively, while the values of energy for the electrolyte with 0% TFA decreased to 4.3 and  $3.8 \text{ mWh cm}^{-3}$  for **ECOF-3** and **ECOF-4**, respectively.

The different behaviors of capacitance, energy, and power allow for an adjustment of the electrolyte composition targeted to the final application. Despite the higher capacitance and energy values obtained with TFA, the devices without TFA are the best choice if high power is required.

In addition, the GCD essays tested the cycling stability. Figure 3C shows the capacitance retention during 10,000 cycles for **ECOF-3**. The behavior was similar for all electrolyte compositions with TFA, losing  $\approx 30\%$  of the capacitance in the first 2,000 cycles and retaining almost 100% between 2,000 and 10,000 cycles. However, only 17% of the capacitance was lost in the first 2,000 cycles for the electrolyte without additive, and almost 100% was retained from then on. In stark contrast, for **ECOF-4** with 20% of TFA, the capacitance increased by 200% during the first 5,000 cycles and then became stable (Figure 3F). This behavior can be attributed to the interaction of the triazine ring and the electrolyte since it can provide extra capacitance, as discussed in our previous work.<sup>[19]</sup> In this case, the pseudocapacitance is a combination between the oxygen of the carbonyl groups and the nitrogen of the triazine ring. Nevertheless, since the nitrogen of the triazine ring is less accessible than the oxygen, it probably needs more time to get the maximum capacitance, which is clearly manifested with the 20% TFA addition. A different behavior was found for **ECOF-4** in the electrolyte with 0% and 5%

TFA. The capacitance increased slightly in the first 1,000 cycles, retaining almost 100% afterwards.

Finally, a higher amount of TFA, 50%, was added to establish the limit of TFA addition that retains a good performance (Figure S34, Supporting Information). In the initial cycles, the capacitance was higher than with 20% TFA, but after 1,000 cycles, the capacitance was completely lost, which suggests that the chemical stability of the material is compromised under these harsh operating conditions.

The energy and power density results of **ECOF-3** and **ECOF-4** show a superior performance compared to other similar COF structures (Table S7, Supporting Information). This is due mainly to the high stability window (3.6 V), obtained by combining organic electrolyte and 20% of TFA, giving rise to a promising performance for high energy and power density applications.

The changes in the performance of the cells due to the addition of TFA were studied by electrochemical impedance spectroscopy (EIS), after 10,000 cycles of charge-discharge. The EIS parameters (Table S8, Supporting Information) of **ECOF-3** and **ECOF-4** with different amounts of TFA were obtained by fitting their Nyquist plots to the corresponding equivalent series circuits (Figure 4; S35, Supporting Information). These values can be used to explain the resistance associated with porous structures (high frequency) and the interaction with the electrolytes (medium-high frequency).

In the high-frequency region of the Nyquist plot of both materials, a semicircle can be observed at all the TFA concentrations. The  $R_A$  element, which represents the contribution of the resistances of the electrolyte, the intrinsic resistance of the electrode and the contact resistance between the electrode and the current collector, can be extracted from the intercept of this circle on the real axis. For **ECOF-3**, this resistance varied between  $6.3 \Omega$  for 0% of TFA and  $4.2 \Omega$  for 20% of TFA, while for **ECOF-4**, it varied between  $3.5 \Omega$  for 0% of TFA to  $3.7 \Omega$  for 20% of TFA. The next resistance,  $R_B$ , is related to the resistance associated with the porous structure; however, when a redox reaction is present, as with the addition of TFA, the interaction between the electrolyte and the redox species could affect the penetration of ions into the pores, thus changing the  $R_B$  value. For **ECOF-3**,  $R_B$  did not suffer significant changes, being  $23 \Omega$  at 0% TFA and  $22 \Omega$  at 20% of TFA. In contrast, the resistance of **ECOF-4** increased significantly with the addition of TFA, increasing from  $23 \Omega$  at 0% of TFA to  $59 \Omega$  with 20% of TFA, suggesting the presence of a redox process in **ECOF-4**.

Below the mid-frequency range (251–160 Hz), there are significant changes associated with the concentration of TFA in the electrolyte. In the absence of TFA, a non-vertical line associated with the ion transport limitation in porous electrodes can be observed, which is well-fitted to a Warburg element. Then, at lower frequencies, the vertical line typical for EDLC corresponds to the ideal capacitive electrode/electrolyte interface, which can be fitted to the constant phase element  $\text{CPE}_{-3}$  in the equivalent series circuit. The fitting yields a near 1 value of the  $n$  constant, which indicates ideal capacitive behavior. In contrast, when 5% TFA is added to the organic electrolyte, the diffusional part at medium frequencies disappeared and the line at low frequencies was no longer vertical, indicating that the redox processes induced a remarkable pseudocapacitive behavior. This is confirmed by the values of  $n$  for  $\text{CPE}_{-3}$  of 0.70 and 0.59 for **ECOF-3** and **ECOF-4**,

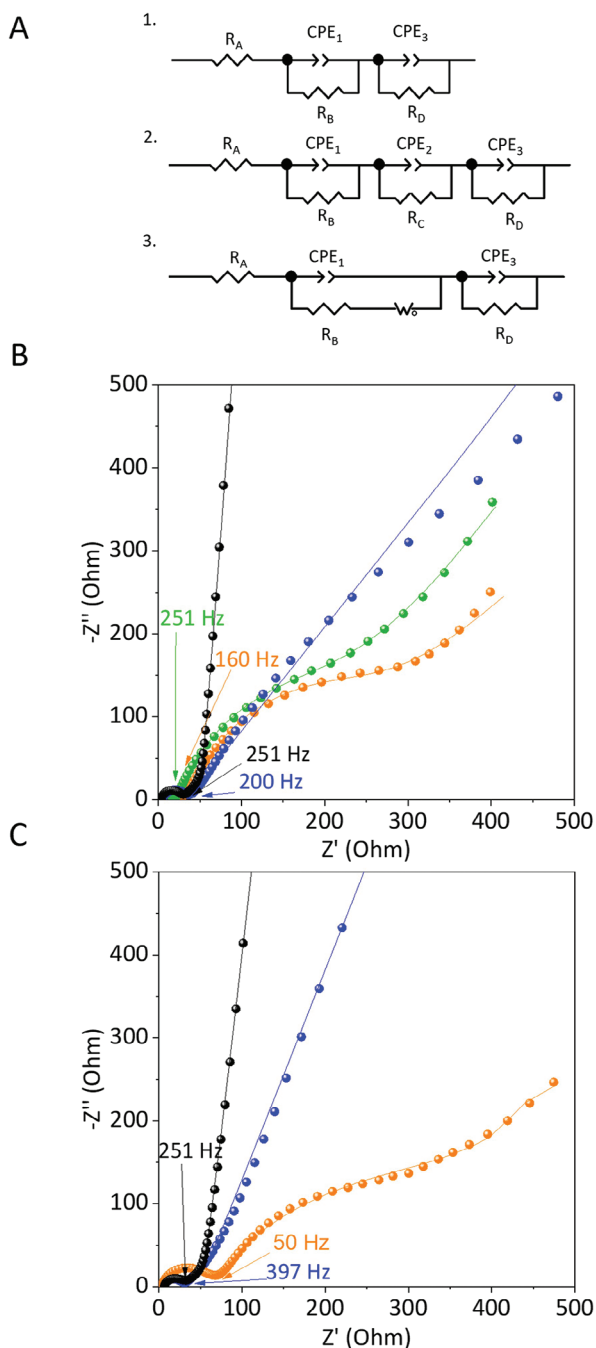


**Figure 4.** Equivalent Series Circuit (ESR) of ECOF-3 and ECOF-4 with 1) 5% TFA, 2) 10–20% TFA and 3) 0% TFA A), Nyquist plot of different electrolytes after 10,000 cycles for ECOF-3 B) and ECOF-4 C). The black line corresponds to 0% TFA, the blue line to 5%, the green line to 10%, and the orange line to 20%. The dots represent the measurements and the lines, the corresponding fitting with the associated equivalent circuit.

respectively. Finally, the addition of higher amounts of TFA (10–20%) led to the appearance of a second semicircle, corresponding to the redox processes previously observed in the galvanostatic charge–discharge experiments. The value of  $R_C$  in the equivalent series circuits can be determined from this second semicircle,

obtaining 146  $\Omega$  for ECOF-3 and 351  $\Omega$  for ECOF-4. The higher value for ECOF-4 is attributed to an increase in the pseudocapacitance, caused by the additional redox reaction at the triazine ring.

These interpretations also agree with the Bode plots shown in Figure S36 (Supporting Information). They show a phase angle close to  $-90^\circ$  for both structures when 0% TFA is used, indicating predominantly capacitive behavior. With the highest amounts of TFA (20%), the phase angle in the lowest frequencies was  $\approx -30^\circ$  indicating a predominantly Faradaic behavior. Finally, with 5% TFA an intermediate behavior was observed, with a phase angle  $\approx -70^\circ$  for ECOF-3 and  $-45^\circ$  for ECOF-4. This difference can be associated with pseudocapacitance due to the interactions between the triazine core and the organic electrolyte.

These EIS results show that different amounts of TFA in the organic electrolyte greatly change the device behavior, going from pure capacitive to pseudocapacitive, while maintaining a potential window of 3.6 V and enhancing the total capacitance and energy density. Additionally, as previously discussed in the GCD results, the main differences between ECOF-3 and ECOF-4 are observed in the presence of 20% TFA. In this case, the  $R_B$  and  $R_C$  elements of the circuit are significantly higher for ECOF-4, and both increases can be associated with the presence of the triazine ring. Specifically, the change in  $R_B$  can be related to slower diffusion of the ions inside the pores due to the interaction of the triazine with the electrolyte, while the two redox centers involved in the pseudocapacitance (the triazine core in addition to the C=O moiety) account for the higher value of  $R_C$ .

### 3. Conclusion

We have demonstrated that the monomer exchange process to transform an imine-linked COF into a partially  $\beta$ -ketoenamine-linked COF can efficiently occur in the gel form, even retaining the monolithic shape. Thus, this room temperature process allows converting the initial imine-linked gel to a  $\beta$ -ketoenamine-linked gel, as a previous step to the formation of the corresponding monolithic  $\beta$ -ketoenamine-linked monolithic aerogels with an excellent conversion ratio (close to 70%). The monolithic porous  $\beta$ -ketoenamine-linked aerogels were fabricated by solvent exchange and  $\text{scCO}_2$  activation processes applied to the  $\beta$ -ketoenamine-linked COF gels.

We have also shown that the mechanical properties of  $\beta$ -ketoenamine-linked COF aerogels allow their transformation into flexible electrodes by a simple compression method.<sup>[10]</sup> Using this method, we fabricated a supercapacitor device based on a composite formed with  $\beta$ -ketoenamine-linked COF aerogel and Carbon Super P, which profits from the  $\beta$ -ketoenamine features of chemical robustness and redox-active sites. The incorporation of  $\beta$ -ketoenamine backbones into the COF structure enables the addition of 20% TFA in the electrolyte, resulting in an enhancement of 90% in the capacitance up to 88  $\text{mF cm}^{-2}$  and excellent stability at a high current density rate (2.0  $\text{mA cm}^{-2}$ ), in comparison to the analogous imine-based COFs.<sup>[19]</sup>

These unprecedented results strongly suggest the new  $\beta$ -ketoenamine-linked COF gels help produce hierarchical porous materials with different shapes and form novel composites that preserve crystallinity and porosity, opening opportunities for COFs in energy-related applications as electrodes and energy storage.

## Supporting Information

Supporting Information is available from the Wiley Online Library or from the author.

## Acknowledgements

J.Á.M., L.S. and A.G.-N. contributed equally to this work. This work was supported by the Spanish Ministry of Science and Innovation, through the “María de Maeztu” Programme for Units of Excellence in R&D (CEX2018-000805-M and CEX2023-001316-M), PDC2022-133498-I00, TED2021-129886B-C42, PID2019-106268GB-C32, PID2022-138908NB-C31, MAT2016-77608-C3-1-P, PCI2018-093081, PID2019-108028GB-C21, and RTI2018-095622-B-I00), and the Catalan AGAUR (project 2017 SGR 238). The authors acknowledge the support from the “(MAD2D-CM)-UAM” project funded by Comunidad de Madrid, the Recovery, Transformation, and Resilience Plan, and NextGenerationEU from the European Union. This work was also funded by the CERCA Program/Generalitat de Catalunya. ICN2 was supported by the Severo Ochoa program from the Spanish MINECO (Grant No. SEV-2017-0706).

## Conflict of Interest

The authors declare no conflict of interest.

## Data Availability Statement

Research data are not shared.

## Keywords

aerogels, covalent organic frameworks, functional COF composites, porous materials, ultralight monolithic aerogels

Received: February 28, 2024

Revised: April 26, 2024

Published online:

- [1] X. Zhao, P. Pachfule, A. Thomas, *Chem. Soc. Rev.* **2021**, *50*, 6871.

- [2] H. Wang, H. Wang, Z. Wang, L. Tang, G. Zeng, P. Xu, M. Chen, T. Xiong, C. Zhou, X. Li, D. Huang, Y. Zhu, Z. Wang, J. Tang, *Chem. Soc. Rev.* **2020**, *49*, 4135.  
 [3] Z. Wang, S. Zhang, Y. Chen, Z. Zhang, S. Ma, *Chem. Soc. Rev.* **2020**, *49*, 708.  
 [4] Y. Su, K. Otake, J.-J. Zheng, S. Horike, S. Kitagawa, C. Gu, *Nature* **2022**, *611*, 289.  
 [5] O. M. Yaghi, *ACS Cent. Sci.* **2019**, *5*, 1295.  
 [6] T. D. Bennett, F.-X. Coudert, S. L. James, A. I. Cooper, *Nat. Mater.* **2021**, *20*, 1179.  
 [7] K. Geng, T. He, R. Liu, S. Dalapati, K. T. Tan, Z. Li, S. Tao, Y. Gong, Q. Jiang, D. Jiang, *Chem. Rev.* **2020**, *120*, 8814.  
 [8] R. Liu, K. T. Tan, Y. Gong, Y. Chen, Z. Li, S. Xie, T. He, Z. Lu, H. Yang, D. Jiang, *Chem. Soc. Rev.* **2021**, *50*, 120.  
 [9] Y. Su, B. Li, H. Xu, C. Lu, S. Wang, B. Chen, Z. Wang, W. Wang, K. Otake, S. Kitagawa, L. Huang, C. Gu, *J. Am. Chem. Soc.* **2022**, *144*, 18218.  
 [10] R.-R. Liang, S.-Y. Jiang, R.-H. A. X. Zhao, *Chem. Soc. Rev.* **2020**, *49*, 3920.  
 [11] Y. Yusran, H. Li, X. Guan, D. Li, L. Tang, M. Xue, Z. Zhuang, Y. Yan, V. Valtchev, S. Qiu, Q. Fang, *Adv. Mater.* **2020**, *32*, 1907289.  
 [12] M. Zhang, L. Li, Q. Lin, M. Tang, Y. Wu, C. Ke, *J. Am. Chem. Soc.* **2019**, *141*, 5154.  
 [13] S. Karak, K. Dey, A. Torris, A. Halder, S. Bera, F. Kanheerampockil, R. Banerjee, *J. Am. Chem. Soc.* **2019**, *141*, 7572.  
 [14] A. K. Mohammed, S. Usgaonkar, F. Kanheerampockil, S. Karak, A. Halder, M. Tharkar, M. Addicoat, T. G. Ajithkumar, R. Banerjee, *J. Am. Chem. Soc.* **2020**, *142*, 8252.  
 [15] J. Á. Martín-Illán, D. Rodríguez-San-Miguel, O. Castillo, G. Beobide, J. Perez-Carvajal, I. Imaz, D. Maspoch, F. Zamora, *Angew. Chem., Int. Ed.* **2021**, *60*, 13969.  
 [16] C. Li, J. Yang, P. Pachfule, S. Li, M.-Y. Ye, J. Schmidt, A. Thomas, *Nat. Commun.* **2020**, *11*, 4712.  
 [17] M. E. Carrington, N. Rampal, D. G. Madden, D. O’Nolan, N. P. M. Casati, G. Divitini, J. Á. Martín-Illán, M. Tricarico, R. Cepitis, C. Çamur, T. Curtin, J. Silvestre-Albero, J.-C. Tan, F. Zamora, S. Taraskin, K. W. Chapman, D. Fairen-Jimenez, *Chem* **2022**, *8*, 2961.  
 [18] M. C. Daugherty, E. Vitaku, R. L. Li, A. M. Evans, A. D. Chavez, W. R. Dichtel, *Chem. Commun.* **2019**, *55*, 2680.  
 [19] J. Á. Martín-Illán, L. Sierra, P. Ocón, F. Zamora, *Angew. Chem., Int. Ed.* **2022**, *61*, e202213106.  
 [20] B. J. Smith, A. C. Overholts, N. Hwang, W. R. Dichtel, *Chem. Commun.* **2016**, *52*, 3690.  
 [21] S.-Y. Ding, J. Gao, Q. Wang, Y. Zhang, W.-G. Song, C.-Y. Su, W. Wang, *J. Am. Chem. Soc.* **2011**, *133*, 19816.  
 [22] J. Dong, Y. Wang, G. Liu, Y. Cheng, D. Zhao, *CrystEngComm* **2017**, *19*, 4899.